Functional Relationships between Kinetic, Flow, and Geometrical Parameters in a High Temperature Chemical Micro-Reactor

M. V. Zagidullin[1,2], R. I. Kaiser[1,3], D. P. Porfiriev [1,2], I. P. Zavershinskiy[1], M. Ahmed[4], V. N. Azyazov*[,1,2] and A. M. Mebel*[,1,5]

[1]*Samara University, Samara 443086, Russia*

[2]*Lebedev Physical Institute of RAS, Samara 443011, Russia*

[3]*University of Hawaii at Manoa, Honolulu, Hawaii, 96822, USA*

[4]*Chemical Sciences Division, Lawrence Berkeley National Laboratory, Berkeley, California 94720, USA*

[5]*Florida International University, Miami, Florida 33199, USA*

Abstract. Computational fluid dynamics (CFD) simulations and isothermal approximation were applied for the interpretation of experimental measurements of the $C_{10}H_7Br$ pyrolysis efficiency in the high-temperature micro-reactor and of the pressure drop in the flow tube of the reactor. Applying isothermal approximation allows the derivation of analytical relationships between the kinetic, gas flow, and geometrical parameters of the micro-reactor which, along with CFD simulations, accurately predict the experimental observations. Based on the obtained analytical relationships, a clear strategy for measuring rate coefficients of (pseudo-)first-order bimolecular and unimolecular reactions using the micro-reactor has been proposed. The pressure- and temperature-dependent rate coefficients for the $C_{10}H_7Br$ pyrolysis calculated using variable reaction coordinate transition state theory (VRC-TST) were invoked to interpret the experimental data on the pyrolysis efficiency.

1. Introduction

Experimental measurements of kinetic rate constants for chemical reactions relevant to processes under typical combustion conditions represent a key challenge for accurate modeling and proper understanding of fuel burning. Only a few percent of reaction rate constants have been measured at the temperatures inherent to combustion. This is due to the insufficient development of experimental instrumentation to carry out kinetic measurements at high temperatures and pressures. A silicon carbide (SiC) chemical micro-reactor incorporated with photoionization mass spectrometry (PIMS) provides an opportunity to measure the kinetic constants of processes under high-temperature conditions up to 2000 K.[1-10] However, several deficiencies of the high-temperature micro-reactor complicate the interpretation of the experimental data. First, gas acceleration and friction against the micro-reactor walls at transonic velocities result in a significant pressure drop and a velocity increase along the flow in the reactor's tube. Second, the wall temperature of the reactor is generally not uniform. Under these conditions, finding dependences of the relative number densities of the reactants and products at the reactor's exit on the residence time of the gas mixture and the number of collisions in the reaction zone is not a simple task. Hence, complex computational fluid dynamics (CFD) simulations in the channel of the micro-reactor accounting for the conservation of mass, momentum balance of the viscous flow, and the heat transfer have to be applied to interpret the experimental data[1,6] and extract subsequent kinetic information. A shock tube technique coupled with PIMS has been also considered for measuring rate constants,[11] but a low cycle rate of the shock tube poses serious problems when recording weak signals, which is common in the studies of kinetic processes. Alternatively, spectroscopic methods to follow the kinetics of reactants, products, and intermediates in a shock tube are broadly used but they require prior knowledge of the spectra of the species involved, which are not universally available.

Guan et al.[1] carried out CFD simulations to explore the gas flow and chemical processes in a micro-reactor in detail. Their analysis of the CFD simulation results has shown that the micro-reactor exhibits several characteristic features in the behavior of the gas flow and its interplay with the chemical kinetics of the reactions involved including the following: a) the gas flow in the reactor is laminar; b) the gas velocity reaches the sonic speed at the exit of the reactor's channel; c) there is a slip of the flow at the boundaries near the downstream end of the reactor under some circumstances; d) the influence of secondary chemical reactions can be minimized. Guan et al.[1] illustrated that the CFD simulation results are comparable with the observed experimental data and concluded that the kinetic information can be extracted by matching CFD

simulations with the concentrations of the reactant and product measured at the reactor's exit. Recently Weddle et al.[12] demonstrated that a boundary-layer model provides a computationally efficient approach to modeling detailed chemical kinetics in the high temperature micro-reactor. They concluded that the flow field depends strongly on the fluid properties of the carrier gas. When Ar used as a carrier, a flow field is far from plug flow. However, a flow field with He as a carrier gas can well be approximated as plug flow.

The CFD simulation provides a great deal of information on distributions of temperature, pressure, velocity, and number densities of the reacting species along the gas flow in the micro-reactor. The results of numerical simulations presented in the literature[1,6,12] show that these distributions may vary dramatically. Fluid dynamic equations take into account both principal and minor interactions and therefore the calculated concentrations of the reactant and product at the reactor's exit depend in a complex manner on the parameters of the reactor and the gas flow. Then, a question arises: Do other strategies exist besides the CFD simulation that can be used to evaluate kinetic constants based on the experimental results measured? When measuring kinetic constants of chemical reactions, handy dependences of the residence time and the number of collisions between reacting species on the flow and the reactor parameters are very much in demand. Finding such dependences would greatly simplify the interpretation of experimental measurements and would allow one to select optimal parameters of the gas flow and the reactor. In the present work, we engage isothermal approximation to derive the dependences of the residence time, the number of collisions, and the output fractions of the components of interest on the flow and reactor parameters in an explicit, analytical form. CFD calculations and flow tube and PIMS measurements are then invoked to validate the obtained analytical dependences by conducting calibration experiments for nitrogen (N_2), oxygen (O_2), carbon dioxide (CO_2), ethylene (C_2H_4), and helium (He). Finally, the developed theoretical expressions are exploited to extract the rate coefficient for unimolecular decomposition of 2-bromonaphthalene (2-$C_{10}H_7Br$) from its output fraction measured experimentally and the results are compared with CFD simulations and with purely theoretical calculations using variable reaction coordinate transition state theory (VRC-TST).

2. Experimental

The gas scheme used for measuring the pressure drop in the tube imitating the SiC chemical reactor at ambient temperature is presented in Figure 1. A Mass-Flow Controller (MFC) GE50A with 200 sccm nitrogen (N_2) full range governed from a personal computer (PC) was used to

control the mass flow rate. The Baratron pressure gauge (Model 722A-23274) measured the gas pressure P_{in} upstream of the tube. Another 275 Convectron Pirani vacuum gauge measured the gas pressure P_{ex} downstream from the tube. Then, a gas channel in the tube with 1.0 mm inner diameter and 2 cm length was drilled in the 9.5 mm steel cylinder. The gas duct was pumped out with a TriScroll vacuum pump (Model TS300). The pumping rate was sufficient to ensure that the pressure of the gas at the tube exit P_{out} was much higher than P_{ex}. The valves V_1, V_2, and V_3 served for redirection of the gas flow or/and separation of some part of the flow from the others. UHP sample gases oxygen (O_2), carbon dioxide (CO_2), ethylene (C_2H_4), and helium (He) were used in this study.

3. Calculations of the rate coefficient for the pyrolysis of $C_{10}H_7Br$

To evaluate the high-pressure limit (HP) rate constants for the barrier-less reactions of the Br atom with 1- and 2-naphthyl radicals $C_{10}H_7$, we employed variable reaction coordinate transition state theory VRC-TST.[13,14] VRC-TST calculations allow evaluating numbers of states for soft transitional modes orthogonal to the reaction coordinate classically, which provides a more accurate result then treating these modes as harmonic oscillators as in the variational TST approach. Within this framework, we computed (*E,J*)-resolved reactive flux for the Br addition to $C_{10}H_7$. The data obtained were then converted to macrocanonical temperature-dependent HP rate constants, which in turn were utilized in master equation calculations of pressure dependence. Energies of various structures were probed at the CASPT2(2,2)/cc-pVDZ level of theory[15,16], where the active space included one unpaired electron of the bromine atom, one unpaired electron of the naphthyl radical $C_{10}H_7$ and the two corresponding orbitals. Then, the following *ad hoc* one-dimensional corrections depending only on the R_{CBr} distance corresponding to the forming C–Br bond were included:

$$E_{rel}[\mathrm{Method}] = E_{rel}[\mathrm{CASPT2(2,2)/cc-pVDZ}] + \Delta E[\mathrm{geom}] + \Delta E[\mathrm{Method}]$$

where E_{rel} is a relative energy for a particular Br/$C_{10}H_7$ configuration with respect to the separated Br + $C_{10}H_7$ fragments. $\Delta E[\mathrm{geom}]$ is a correction for geometry relaxation computed as a difference of energies of an optimized structure along the minimum energy path (MEP) for the approaching fragments corresponding to a particular value of R_{CBr} and the structure at the same R_{CBr} but with geometry of the $C_{10}H_7$ fragment frozen (the same as in an isolated $C_{10}H_7$ radical). The calculations of $\Delta E[\mathrm{geom}]$ were carried out at the CASPT2(2,2)/cc-pVDZ level. The geometry optimization was not complete because all the dihedral angles were kept frozen at 0° or 180° to ensure C_s symmetry of the structure. $\Delta E[\mathrm{Method}]$ is a correction for a higher level of

theory computed for frozen-fragment structures along the MEP also corresponding to particular values of R_{CBr}:

$$\Delta E[\text{Method}] = E_{rel}[\text{Method}] - E_{rel}[\text{CASPT2}(2,2)/\text{cc} - \text{pVDZ}]$$

The higher-level corrections were evaluated at the CASPT2 level with the same (2,2) active space and the cc-pVTZ ($E_{\text{cc}-\text{pVTZ}}$) and cc-pVQZ ($E_{\text{cc}-\text{pVQZ}}$) basis sets. The calculated values were then used for extrapolation to the complete basis set (CBS) limit using the two-point expressions

$$E_{\text{CBS}} = E_{\text{cc}-\text{pVQZ}} + \left(E_{\text{cc}-\text{pVQZ}} - E_{\text{cc}-\text{pVTZ}}\right) \times 0.69377$$

$$E_{\text{CBS}} = E_{\text{cc}-\text{pVTZ}} + \left(E_{\text{cc}-\text{pVTZ}} - E_{\text{cc}-\text{pVDZ}}\right) \times 0.46286$$

The corrections were computed at finite values of R_{CBr} between 1.6 and 8 Å and then an interpolation by splines was employed to evaluate the corrections at arbitrary R_{CBr} values within the given range. All the ab initio calculations were performed using the GAUSSIAN 09[17] and MOLPRO 2010[18] program packages.

On the course of VRC-TST calculations, the corrections were added to the explicitly computed energy of a configuration based on the R_{CBr} value in this configuration. In the case of 1-bromonaphthalene (Figure 2), there was only small difference between two values obtained using the aforementioned expressions at lengths from the range of interest ($R_{\text{CBr}} \approx 1.9$ Å and higher in the $C_{10}H_7Br$ molecules), so the extremely demanding computations with the cc-pVQZ ($E_{\text{cc}-\text{pVQZ}}$) basis set were not carried out for 2-bromonaphthalene. Bond dissociation energies used in ME-analysis were set to 81.2 kcal/mol and 81.7 kcal/mol for 1- and 2-bromonaphthalene respectively.[19] Calculated rate constants for unimolecular dissociation of 1- and 2-bromonaphthalene to $C_{10}H_7$ + Br are presented in Figure 3 (a) and (b), respectively.

Rate constant values were approximated by modified Arrhenius expressions and used in numerical simulations. The list of reactions significant for the modeling of the 2-$C_{10}H_7Br$ pyrolysis is presented in Table 1. The pressure dependence of k_{1f} was approximated as logarithmic. Rate constants of the secondary reactions 2 and 3 were taken from the literature.[20,21] Modified Arrhenius expressions for the rate constants, geometries and frequencies employed for rate constant calculations, as well as optimized geometries along the MEP are given in Supporting Information.

4. Results and Discussion

4.1. CFD simulation results

In this section, we present the velocity, pressure, temperature and reactive species distributions in the reactor computed by solving the Navier-Stokes equations for the conservation

of mass, momentum balance for the viscous flow, and the heat transfer reported elsewhere.[1,6,8,10] Usually, in experiments the reactive species were greatly diluted with a carrier gas and so we can ignore the effect of chemical reactions on the dynamics of the flow. The Comsol-Multiphysics package[22] was employed for the calculation of the distribution of gas-dynamic parameters of the gas flow in the micro-reactor. When simulating physicochemical processes in the micro-reactor, the following problems were simultaneously solved: the flow of the electric current and ohmic heating, the heat transfer between the nodes of the micro-reactor and the radiative heat transfer to the surrounding space, the Navier-Stokes and heat-mass transfer problems in the gas flow, the kinetics of the pyrolysis process. The temperature dependences of the viscosity, heat conductivity, and heat capacity in the range of T = 300-1600 K were taken into account. For the mass flow used, the gas pressure closer to the exit of the reactor can be less than 10 Torr. Under these conditions with the He carrier gas there is a slip of the flow at the boundaries.[1,6] The Maxwell model for the slip velocity boundary conditions at the wall of the reactor was employed. It should be noted that this group recently employed the approach described above to CFD simulations of physical and chemical processes in the micro-reactor while studying the *ortho*-biphenylyl radical plus acetylene[6] and phenyl radical plus vinylacetylene[23] reactions and found a generally good agreement with experiment.

The initial data for the calculations correspond to the experimental conditions reported in detail in our recent publication[24] and presented in Table 2. A simplified sketch of a resistively-heated silicon-carbide (SiC) high-temperature 'chemical reactor' used in this work is shown in Figure 4. The microrector represents a gas-flow SiC tube with an internal diameter of 1 mm, total length of 38 mm, and ohmic heating zone length of 20 mm. The temperature of the SiC tube was monitored using a type-C thermocouple. The inlet end of the SiC tube (2 mm in length) was inserted into a hole in the alumina holder, which in turn was surrounded by a copper heat-exchanger cooled by water. Molybdenum electrodes with a diameter of 21 mm and a width of 4 mm come into contact with the SiC tube through graphite slivers. The carrier gas and pyrolysis products flow into the zone of strong rarefaction (pressure below 10^{-6} torr). After exiting the pyrolytic reactor, the molecular beam passes a skimmer and enters a detection chamber containing a ReTOF mass spectrometer. The products were photoionized in the extraction region of the spectrometer by exploiting quasi continuous tunable vacuum ultraviolet (VUV) light from the Chemical Dynamics Beamline of the Advanced Light Source and detected with a microchannel plate detector.

In the first approximation, the temperature distribution obtained by solving the heat-transfer problem only for solid parts of the reactor was employed to start CFD calculations. The ohmic heating power was adjusted so that to achieve the reactor wall temperature of T_c±1 K at

the center point between the electrodes. Next, ohmic heating, heat transfer, non-isothermal CFD, and mass transfer problems were solved simultaneously by the iterative method. In the iteration procedure, the gas pressure at the outlet of the reactor and ohmic heating power were considered as independent variables at a preset mass flow rate. The initial values of the variables for the iteration step N+1 were taken from the previous step N. The gas outlet pressure and ohmic heating were varied until the Mach number value of $M = 1 \pm 0.01$ at some point of the outlet cross section of the reactor and the wall temperature $T_c \pm 1$ were attained.

The distributions of temperature T, pressure P, and gas velocity U_0 along the tube at the central axis of the reactor for T_c = 1500 K are presented in Figure 5. Analogous modeling was also performed at the electric power of 48 W at which the micro-reactor's temperature was T_c = 1600 K. Calculations show that the distributions of the radial temperature and number densities of the gas components are almost uniform in the high-temperature region of the reactor. The heating power of 37 W at T_c = 1500 K is mainly lost via radiative emission (33 W) from the SiC tube, graphite slivers, and molybdenum electrodes. A small part (3 W) of the heat power leaks through the alumina holder. The rest of the heat (1W) is carried away with the gas flow.

The temperature distribution in the SiC reactor between the electrodes is determined from the balance of the energy input during the resistive heating and energy removal both during the heat transfer along the tube and thermal radiation from the surface of the tube and electrodes. Figure 5 displays the temperature dependence for the SiC tube with the assumed heat conductivity λ = 12 W m^{-1} K^{-1}, T_c = 1500 K (solid curve), whereas the dashed curve shows the temperature distribution for a ZrO_2 tube with λ = 2 W m^{-1} K^{-1}.[25] Clearly, in the case of a ZrO_2 tube, the reactor temperature is nearly uniform along almost the entire interval of the tube between the electrodes that should be conductive for measuring kinetic constants in the reactor.

CFD calculations of pressure P, temperature T and axis velocity U_0 distribution as well as the rate constants presented in Table 1 (including those for forward and reverse 2-$C_{10}H_7Br \rightarrow C_{10}H_7$ + Br reactions computed here) were used to compute the 2-$C_{10}H_7Br$ pyrolysis efficiency for two wall temperatures of the SiC tube between electrodes. The results of the calculations are presented in Figure 6. According to the results, the pyrolysis efficiency of 2-bromonaphthalene was about 15% at 1500 K and 46% at 1600 K. One has to take into account the accuracy of the rate constant calculations within a factor of 2[26] and the accuracy of the micro-reactor's temperature (1-2%) and flow rate (±4%) measurements. Taking these points into consideration, we can conclude that the experimentally observed[24] pyrolysis efficiency of 40% at T_c = 1500 K is in good agreement with the results of calculations of the pyrolysis efficiency (15-46%). The

uncertainty in the calculated data is mainly due to the allowable range of values T_c±1 and M = 1±0.01 in the iterative procedure and does not exceed 1%.

The pressure drop and the velocity increase together with the temperature decrease along the flow at $z \geq 2.8$ cm causes the pyrolysis process to stop as can be seen from the results presented in Figure 6. We can also see from this Figure that the pyrolysis of 2-$C_{10}H_7Br$ occurs in the range from z_1 = 18 mm to z_2 = 28 mm. In this reaction zone the gas temperature varies within narrow limits $T \approx 1450 \div 1500$ K. The average residence time calculated using the equation derived previously (Eq. S7 in Ref.[6]) at the experimental conditions (T = 1500 K) in the z-interval [18 mm, 28 mm] of the reactor amounts to τ_{res} = 56 μs.

These CFD calculations illustrate that the rate constant for the 2-$C_{10}H_7Br$ pyrolysis can be derived from the measured pyrolyzed fraction of $C_{10}H_7Br$ at the exit of the reactor by matching the simulation result to experiment achieved through adjustment of the assumed rate constant expression; here, the assumed rate constant expression was obtained from the first-principles VRC-TST calculations. It should be also noted that the result for the pyrolysis efficiency in the present case appears to be not sensitive with respect to the assumed rate constants for the secondary reactions of the formation and dissociation of Br_2. In the consequent Section, we consider how the rate constant can be evaluated more directly, without CFD simulations.

4.2. Isothermal approximation

Acceptable accuracy in measurements of kinetic constants having strong temperature dependence can be attained if the temperature between electrodes is close to uniform. The CFD calculation results show that this can be achieved by using the material for the tube of the reactor with low thermal conductivity and with an appropriate design of the electrodes. In this case, the chemical reaction under consideration would take place under nearly uniform conditions and one can obtain rather simple and clear dependences of the residence time and the number of collisions in the reaction zone on the parameters of the reactor and the gas flow using the following assumptions:

- The gas flow is laminar and isothermal;
- There are no pressure and temperature gradients across the flow (fast heat and momentum transverse transport);
- Number density of each component is uniform across the flow (fast transverse diffusion)
- The velocity profile across the flow is parabolic throughout the reactor length;
- The centerline gas velocity at the outlet edge of the reactor is sonic;

- There is no slip of the gas stream at the surface of the reactor.

Then, the gas mass flow rate g can be expressed as

$$g = \int_0^{d/2} 2\pi y U(z) \frac{P(z)}{RT}\left(1 - \left(\frac{2y}{d}\right)^2\right) dy = s\frac{P(z)U(z)}{2RT} \quad (1)$$

Here, U is the centerline axial velocity, $P(z)$ is the gas pressure at distance z from the inlet edge of reactor, R(J kg^{-1} K^{-1}) = 8.31/M is the gas constant, M(kg /mol) is the molecular weight of the gas mixture, $s = \pi d^2/4$ is the geometric cross-section of the gas channel, d is the internal tube diameter, and T is the gas temperature. In particular, the pressure of the gas at the reactor exit is equal to

$$P_{out} = \frac{2gRT}{sc} = \frac{2gc}{\gamma s}, \quad (2)$$

where $c = \sqrt{\gamma RT}$ is the sonic velocity at temperature T and γ is the heat capacity ratio.

The total momentum I of the gas stream can be found as follows

$$I = \int_0^{d/2} 2\pi y\left(P(z) + \frac{U^2(z)P(z)}{RT}\left(1 - \left(\frac{2y}{d}\right)^2\right)^2\right) dy = P(z)s\left(1 + \frac{U^2(z)}{3RT}\right) \quad (3)$$

The pressure drop is due to the viscous force at the surface, which is equal to $4\pi U_0\mu$ per unit of length along the tube. Then, one obtains the equation for the momentum[27]

$$\frac{dI}{dz} = -4\pi\mu U, \quad (4)$$

where μ is the viscosity coefficient. Taking into account Eqs. (1)-(3), the solution of the differential equation (4) is given by

$$P(z)^2 - P_{out}^2\left(1 + \frac{4\pi\gamma\mu(L-z)}{g}\right) - \frac{2\gamma P_{out}^2}{3} ln\left(\frac{P(z)}{P_{out}}\right) = 0, \quad (5)$$

where L is the total length of the reactor. Using Eqs. (2) and (5) together, we can find the pressure distribution $P(z)$ along the flow in the reaction zone. In practically interesting cases, the condition $\frac{4\pi\gamma\mu L}{g} >> 1$ is valid. In this case, Eq. (5) can be rewritten as follows[28]

$$P(z) = P_{out}\sqrt{1 + \frac{4\pi\gamma\mu(L-z)}{g}} = \frac{2\cdot g\cdot R\cdot T}{s\cdot c}\sqrt{1 + \frac{4\pi\gamma\mu(L-z)}{g}} \quad (6)$$

It follows from Eq. (6) that the gas pressure at the inlet of the reaction zone (z = 0) is given by

$$P_{in} = \sqrt{\left(\frac{g\cdot RT}{0.5c\cdot s}\right)^2 + \frac{16\mu\cdot R\cdot T\cdot\pi\cdot g}{s^2}L} \quad (7)$$

The assumptions made above can be critical for finding target parameters under conditions of transonic velocities at low outlet pressures. In this Section we present experimental and CFD calculated results indicating that isothermal approximation can be applied for finding relationships between the flow and the reactor parameters. Using the gas-flow testing line shown in Fig. 1, the inlet gas pressures (z = 0) were measured in relation to the molar flow rates of CO_2 and He at ambient temperature which are depicted with black square symbols in Figures 7 and 8. Blue triangle symbols in these Figures represent the results of CFD simulations at the experimental conditions. For further CDF and analytical calculations we used the values of viscosity and heat capacity ratios presented in Table 3. Simplified $T^{0.5}$ temperature dependences[29] of gas viscosity coefficients were utilized and heat capacity ratios were computed using the temperature dependence of the gas heat capacity.[25] One can see that both CFD and analytical calculations satisfactory reproduce the experimental data in the wide range of variation of the gas flow rate of O_2, C_2H_4, CO_2, and He. This testifies to the validity of our assumptions adopted in the beginning of this Section.

Typical pressure distributions along the flow calculated using Eqs. (5) and (6) along with CFD simulations are exhibited in Figure 9 at T = 1500 K and the molar flow rate g = 400 sccm for two carrier gases C_2H_4 and He. CFD calculations were carried out at a constant temperature of the reactor wall, although the gas temperature closer to the outlet of the reactor was slightly decreased. The differences between the three calculated pressure distributions do not exceed 10 % all the way from the entrance to the exit of the reaction zone. The lighter the carrier gas and the lower the gas flow rate, the higher the ratio $\varepsilon = P_{in}/P_{out}$. For example, for the conditions of Fig. 9, the values of ε amount to 1.57 and 5.24 for C_2H_4 and He, respectively. For g = 50 sccm and T = 1500 K, the values of ε are 3.2 and 16.9 for C_2H_4 and He, respectively. Thus, the most uniform pressure distribution can be achieved with heavier carrier gases at higher flow rates but the latter condition represents a technical challenge.

As mentioned above, the pressure distributions calculated by CFD and via Eqs. (5) and (6) are very similar. At isothermal conditions, this means that the average velocity distributions along the z axis are also very similar. The distribution from Eq. (6) exhibits a clear analytical dependence on the reactor and gas flow conditions, allowing us to obtain the most important parameters such as the gas residence time, the number of collisions of a molecule with ambient molecules, and the consumption of reacting components. It is more convenient to derive the formulas of interest using the distance from the outlet of the reactor $y = L - z$. The gas residence time inside the interval $[y_1, y_2]$ in isothermal approximation can be expressed as follows[6]

$$\tau_{res}(y_1, y_2) = \int_{z_1}^{z_2} \frac{P(z)S}{gRT}\, dz = \frac{2}{c}\int_{y_2}^{y_1} \sqrt{1 + \frac{4\pi\gamma\mu y}{g}}\, dy \qquad (8)$$

where $y = L - z$, $y_1 = L - z_1$, $y_2 = L - z_2$ are distances from the reactor outlet and $y_1 > y_2$. Substitution of Eq. (6) into Eq. (8) and integration of the resulting expression gives an analytical formula for the residence time

$$\tau_{res}(y_1, y_2) = \frac{g}{3\pi c\gamma\mu}\left(\left(1 + \frac{4\pi\mu c^2}{g \cdot R \cdot T} y_1\right)^{1.5} - \left(1 + \frac{4\pi\mu c^2}{g \cdot R \cdot T} y_2\right)^{1.5}\right) \quad (9)$$

Taking into account that $c = \sqrt{\gamma RT}$ one obtains

$$\tau_{res}(y_1, y_2) = \frac{g}{3\pi\gamma^{1.5}(RT)^{0.5}\mu}\left[\left(1 + \frac{4\pi\mu\gamma}{g} y_1\right)^{1.5} - \left(1 + \frac{4\pi\mu\gamma}{g} y_2\right)^{1.5}\right] \quad (10)$$

It is remarkable that there is no dependence of the residence time on the reactor diameter *d*. Using Eq. (10) the dependences of residence time τ_{res} on the gas temperature *T*, the interval [y_1, y_2] of the reaction zone, the gas flow rate *g*, and the molecular weight of the gas mixture *M* can be easily traced. To calculate the total gas residence time in the reactor one has to make a substitution $y_1 = L$, $y_2 = 0$ in Eq. (10).

The dependences of the residence time on the gas flow rates of He, C_2H_4, and CO_2 with the reaction zone length L = 1 cm and the gas temperature of 1000 K are shown in Figure 10 as an example. As can be seen, a fast decrease in the residence time with the gas flow rate occurs for the gas flow rates below 100 sccm and then the residence time drops only moderately at higher values of the flow rate. For instance, with an increase in the gas flow rate from 200 to 400 sccm τ_{res} falls by only about 20%. Using He as a carrier gas is preferable because this allows one to obtain lowest values of the residence time. The residence time calculated using Eq. (10) for the interval [y_1 = 2 cm, y_2 = 1 cm or z_1 = 1.8 cm, z_2 = 2.8 cm] at the experimental conditions for the 2-$C_{10}H_7Br$ pyrolysis, T = 1500 K, $g = 2.46\times10^{-4}$ g/s, $\mu = 4.4\times10^{-4}$ g/(cm s) amounts to τ_{res} = 67 μs, in satisfactory agreement with the CFD calculated result.

The number of collisions of reacting species is one of the important parameters necessary for evaluating kinetic constants. Using the known distribution of the gas pressure determined by Eq. (6), the number *N* of collisions of a selected molecule with ambient molecules in the interval [y_1, y_2] zone is given by

$$N(y_1, y_2) = k\int_{\tau_{res}(y_2,0)}^{\tau_{res}(y_1,0)} n\, d\tau_{res} = k\frac{4g(y_1 - y_2)}{\gamma k_B T s}\left[1 + \frac{2\gamma\pi\mu}{g}(y_1 + y_2)\right], \quad (11)$$

where *k* is a rate constant in the gas-kinetic collision limit (~10^{-10} cm^3/s), $n = \frac{P(y)}{k_B T}$ is the total number density, k_B is Boltzmann constant. For example, at the experimental conditions for the 2-

$C_{10}H_7Br$ pyrolysis, the calculations give the number of collisions N = 708 in the interval $[y_1,y_2]$ = [2 cm,1 cm].

Finally, let us derive the expressions that relate the fraction of a component A reacting in a bimolecular reaction A + B having rate constant k_{AB} in a carrier gas C. The subject of interest is a change of the value $\eta_A = n_A/n$ at when gas flows from the distance z_1 to the distance z_2 in the reactor. Here n_A and n_C denote the number densities of the component A and the carrier gas, respectively. It is assumed that numbers density of the components A, B and C are in the relation $n_C >> n_B >> n_A$. The balance rate equation for a pseudo-first order bimolecular reaction A + B under our assumptions has the following form

$$-\frac{d}{dz}\eta_A = \frac{d}{dy}\eta_A = k_{AB}(\eta_B n)(\eta_A n)\frac{Ms}{N_A g}, \qquad (12)$$

where $\eta_B = n_B/n$, $n = n_A + n_B + n_C$, N_A is Avogadro number. The solution of Eq. (12) is given by

$$ln\frac{\eta_A(y_2)}{\eta_A(y_1)} = -\frac{k_{AB}\eta_B Ms}{gN_A}\int_{y_2}^{y_1}\left(\frac{P(y)}{k_B T}\right)^2 dy \qquad (13)$$

By integrating Eq. (13) we obtain the following expression relating the fraction of the component A to the parameters of the reactor and the gas flow within the distance from y_1 to y_2

$$\frac{\eta_A(y_2)}{\eta_A(y_1)} = \exp\left(-\frac{k_{AB}\eta_B N(y_1,y_2)}{k}\right) = exp\left\{-k_{AB}\eta_B\frac{4g(y_1-y_2)}{\gamma k_B Ts}\left[1+\frac{2\gamma\pi\mu}{g}(y_1+y_2)\right]\right\} \qquad (14)$$

where $N(y_1,y_2)$ is defined by Eq. (11). The physical meaning of Eq. (14) is quite clear. The value k_{AB}/k is the probability of the reaction A + B to occur in a single collision, $\eta_B N(y_1, y_2)$ is the number of collisions of a molecule A with molecules B in the interval $[y_1, y_2]$.

For a unimolecular reaction AB $\rightarrow$ A + B with a pressure independent rate coefficient k_{AB} (s^{-1}) the change of the AB fraction in the interval $[y_1, y_2]$ is

$$\frac{\eta_A(y_2)}{\eta_A(y_1)} = exp\left(-k_{AB}\tau_{res}(y_1,y_2)\right) =$$

$$= exp\left[-\frac{k_{AB}g}{3\pi\gamma^{1.5}(RT)^{0.5}\mu}\left[\left(1+\frac{4\pi\mu y_1\gamma}{g}\right)^{1.5}-\left(1+\frac{4\pi\mu y_2\gamma}{g}\right)^{1.5}\right]\right] \qquad (15)$$

Let us estimate the efficiency of 2-$C_{10}H_7Br$ decomposition using Eq. (15). We assume that pyrolysis occurs only within the distance interval z_1 = 1.8 cm (y_1 = 2 cm) to z_2 = 2.8 cm (y_2 = 1 cm) and the temperature is 1500 K. This assumption is reasonable because COMSOL calculations showed explicitly that efficient decomposition of 2-$C_{10}H_7Br$ occurs in this interval (see Fig. 6). The calculation with the numerical values of the viscosity $\mu = 4.44\times10^{-4}$ g cm^{-1} s^{-1}

(Table 3), the rate constant of 2-$C_{10}H_7Br$ decomposition $k_{AB} = k_{fP1} = 1.52\times10^3$ s^{-1} at T = 1500 K (Table 1) gives $\frac{\eta_A(y_2)}{\eta_A(y_1)}$ = 0.90 or the efficiency of decomposition of 10%. This is in good agreement with the CFD-calculated result 13% (Fig. 6), but lower than the experimental value of 40% at 1500 K. The discrepancy with experiment can be due to underestimation of the value of k_{fP1} in the quantum chemical calculations. Another possible reason for this discrepancy can be an underestimation of the reactor's temperature. The temperature measurement in the reactor is a complex problem and a substantial uncertainty of this value can be expected. The rate constant sharply depends on temperature and this uncertainty can result in incorrect interpretation of the experimental result. For example, at the temperature T = 1600 K, $k_{fP1}= 8.45\times10^3$ s^{-1} and Eq. (14) gives 43% for the efficiency of the 2-$C_{10}H_7Br$ pyrolysis. This is in excellent agreement with the CFD calculations (46%). This estimation is closer to the experimentally measured efficiency of 40%, which forces us to assume that the real temperature of the reactor was closer to 1600 K.

5. Conclusions

Summarizing, we can conclude that the high-temperature micro-reactor can be used to measure kinetic constants of processes that last more than a few tens of microseconds. The results of CFD simulations testified (Fig. 5, dashed curve) that temperature distribution over most of the reactor interval between the electrodes can be nearly uniform for tubes with low values of thermal conductivity coefficients $\lambda \leq 2$ W m^{-1} K^{-1}. In this case, isothermal approximation can be applied for the interpretation of experimental data. By neglecting the pressure, temperature, and component concentrations gradients across the flow, assuming a parabolic velocity profile throughout the reactor length, taking the centerline gas velocity at the outlet of the reactor to be equal to sonic, and neglecting slip of the gas velocity at the surface of the reactor, the analytical equations for the residence time (Eq. (9)), the number of collisions (Eq. (11)), relative fractions of components of interest at the reactor exit (Eq. (14) for bimolecular reactions and Eq. (15) for unimolecular reactions) have been derived. The calculated values of the efficiency of the 2-$C_{10}H_7Br$ pyrolysis using Eq. (15) and CFD simulations are in satisfactory agreement. Even better agreement has been obtained between the calculated and experimental values of the inlet pressure P_{in} as illustrated on Figs. 7 and 8. This confirmed that the assumptions taken are judiciously chosen. We are not aware of any reports in which the kinetic measurements were carried out in a micro-reactor with a temperature distribution close to constant over a greater part of the reaction zone. This did not allow us to test the proposed

approach to the fullest, but further verification of the isothermal approximation should become possible with new developments of the experimental technique.

At a low He flow rate, the free path becomes comparable with the tube radius and a flow slip occurs at the boundaries near the downstream end of the tube. This effect was taken into account in CFD simulations but was neglected when analytical expressions were deduced. CFD calculations reveal that there is a significant increase of slip velocity up to about 400 m/s closer to the exit of the tube. If this effect becomes significant only in a short interval, then it can be neglected, especially at elevated gas flow rates.

As follows from Fig. 10, the residence time shortens with a gas flow rate, dropping rapidly up to about 100 sccm and then decreases moderately. High values of τ_{res} at low gas flow rates are due to large pressure losses via friction. Therefore, measurements of kinetic constants of fast processes should be preferably carried out at elevated gas flow rates above 100 sccm. With such flow rates, a pulsed gas supply mode is worthy of consideration. It should be noted however that CFD calculations are difficult with pulsed flows and need be performed with special care. Alternatively, the analytical expressions derived here within isothermal approximation can be applied for the pulse mode when the time required to reach a quasi-stationary gas flow, L/c, is shorter than the pulse duration.

Eqs. (14) and (15) make it possible to easily interpret the experimental data and extract the values of the rate coefficients for (pseudo-)first-order ($n_B >> n_A$) bimolecular and unimolecular reactions, respectively. For example, a linear fit of an experimental plot of $ln\,\eta_A(y_2)/\eta_A(y_1)$ vs. η_B at a fixed gas temperature and $\eta_A \ll \eta_B \ll 1$ allows one to determine the rate coefficient, as follows from Eq. (14). The rate coefficient for a unimolecular process can then be extracted from experimental dependences of $ln\,\eta_A(y_2)/\eta_A(y_1)$ on the reactor length L or the total gas flow rate g using Eq. (15). The more uniform the temperature distribution in the reaction zone, the higher the accuracy of the measurement. Thus, the micro-reactor can be employed for direct measurements of reaction rate constants, especially when secondary reactions are too slow to affect the consumption and production of the component of interest.

AUTHOR INFORMATION

Corresponding Authors

Email: Azyazov@rambler.ru.

Email: Mebela@fiu.edu.

The authors declare no competing financial interest.

Supporting Information. Modified Arrhenius expressions for rate constants, geometries and frequencies employed for rate constant calculations, optimized geometries along the MEP for 1-bromonaphthalene, and optimized geometries along the MEP for 2-bromonaphthalene.

Acknowledgments

This work was supported by the Ministry of Education and Science of the Russian Federation under the Grant No. 14.Y26.31.0020 to Samara University. RIK acknowledges support from the U.S. Department of Energy, Basic Energy Sciences DE-FG02-03ER15411 for the calibration studies and the pyrolysis experiments. MA is supported by the Director, Office of Science, Office of Basic Energy Sciences, of the U.S. Department of Energy under Contract No. DE-AC02-05CH11231, through the Gas Phase Chemical Physics program of the Chemical Sciences Division. AMM's work at FIU is supported by the U.S. Department of Energy, Basic Energy Sciences DE-FG02-04ER15570.

References

(1) Guan, Q.; Urness, K. N.; Ormond, T. K.; David, D. E.; Barney Ellison, G.; Daily, J. W. The Properties of a Micro-Reactor for the Study of the Unimolecular Decomposition of Large Molecules *Int. Rev. Phys. Chem.* **2014**, *33*, 447-487.

(2) Chen, P.; Colson, S. D.; Chupka, W. A.; Berson, J. A. Flash Pyrolytic Production of Rotationally Cold Free Radicals in a Supersonic Jet. Resonant Multiphoton Spectrum of the $3p^2A_2'' \leftarrow X^2A_2''$ Origin Band of Methyl. *J. Phys. Chem.* **1986**, *90*, 2319-2321.

(3) Parker, D. S. N.; Kaiser, R. I.; Troy, T. P.; Kostko, O.; Ahmed, M.; Mebel, A. M. Toward the Oxidation of the Phenyl Radical and Prevention of PAH Formation in Combustion Systems. *J. Phys. Chem. A.* **2014**, *119*, 7145-7154.

(4) Kohn, D. W.; Clauberg, H.; Chen P. Flash Pyrolysis Nozzle for Generation of Radicals in a Supersonic Jet Expansion. *Rev. Sci. Instrum.* **1992**, *63*, 4003-4005.

(5) Zhang Y.; Cai, J; Zhao, L.; Yang, J.; Jin, H.; Cheng, Z.; Li, Y.; Zhang, L.; Qi, F.; An Experimental and Kinetic Modeling Study of Three Butene Isomers Pyrolysis at Low Pressure. *Combust. Flame*. **2012**, *159*, 905-917.

(6) Yang, T.; Kaiser, R. I.; Troy, T. P.; Xu, B.; Kostko, O.; Ahmed, M.; Mebel, A. M.; Zagidullin, M. V.; Azyazov, V. N. HACA's Heritage: A Free-Radical Pathway to Phenanthrene in Circumstellar Envelopes of Asymptotic Giant Branch Stars. *Angew. Chem., Int. Ed.* **2017**, *56*, 4515-4519.

(7) Zhang, X.; Friderichsen, A. V.; Nandi, S.; Ellison, G. B.; David, D. E.; McKinnon, J. T.; Lindeman, T. G.; Dayton, D. C.; Nimlos, M. R. Intense, Hyperthermal Source of Organic Radicals for Matrix-Isolation Spectroscopy. *Rev. Sci. Instrum.* **2003**, *74*, 3077-3086.

(8) Ni, C.-K.; Huang, J. D.; Chen, Y. T.; Kung, A. H.; Jackson, W. M. Photodissociation of Propyne and Allene at 193 nm with Vacuum Ultraviolet Detection of the Products. *J. Chem. Phys.* **1999**, *110*, 3320-3325.

(9) Taatjes, C. A.; Hansen, N.; McIlroy, A.; Miller, J. A.; Senosiain, J. P.; Klippenstein, S. J.; Qi, F.; Sheng, L.; Zhang, Y.; Cool, T. A.; et al. Chemistry: Enols are Common Intermediates in Hydrocarbon Oxidation. *Science*, **2005**, *308*, 1887-1889.

(10) Guan, Q.; Ellison, G. B.; Stanton, J. F.; Ahmed, M.; Daily, J. W. DSMC Simulations of a Photoionization Mass Spectrometer. *54th AIAA Aerospace Sciences Meeting*, **2016**, 160339.

(11) Tranter, R. S.; Lynch, P. T. A Miniature High Repetition Rate Shock Tube. *Rev. Sci. Instrum.*, **2013**, *84*, 094102.

(12) Weddle, P. J.; Karakaya, C.; Zhu, H.; Sivaramakrishnan, R.; Prozument, K.; Kee, R. J. Boundary-Layer Model to Predict Chemically Reacting Flow within Heated, High-Speed, Microtubular Reactors. *Int. J. Chem. Kin.* **2018**, *50*, 473-480.

(13) Georgievskii, Y.; Klippenstein, S.J. Transition State Theory for Multichannel Addition Reactions: Multifaceted Dividing Surfaces. *J. Phys. Chem. A.* **2003**, *107*, 9776–9781.

(14) Georgievskii, Y.; Klippenstein, S.J. Variable Reaction Coordinate Transition State Theory: Analytic Results and Application to the $C_2H_3 + H \rightarrow C_2H_4$ Reaction. *J. Chem. Phys*. **2003**, *118*, 5442–5455.

(15) Celani, P.; Werner, H.-J. Multireference Perturbation Theory for Large Restricted and Selected Active Space Reference Wave Functions. *J. Chem. Phys.* **2000**, *112*, 5546-5557.

(16) Shiozaki, T.; Gyorffy, W.; Celani, P.; Werner, H.-J. Communication: Extended Multi-State Complete Active Space Second-Order Perturbation Theory: Energy and Nuclear Gradients. *J. Chem. Phys*. **2011**, *135*, 081106.

(17) Frisch, M. J.; Trucks, G.W.; Schlegel, H. B.; Scuseria, G. E.; Robb, M. A.; Cheeseman, J. R.; Scalmani, G.; Barone, V.; Mennucci, B.; Petersson, G. A.; et al. *Gaussian 09, Revision D.01*; Gaussian, Inc.: Wallingford, CT, 2009.

(18) Werner, H.-J.; Knowles, P. J.; Lindh, R.; Manby, F. R.; Schütz, M.; Celani, P.; Korona, T.; Mitrushenkov, A.; Rauhut, G.; Adler, T. B.; et al. *MOLPRO, Version 2010.1, a Package of Ab Initio Programs*; University of Cardiff: Cardiff, U.K., 2010.

(19) Luo, Y.-R. *Comprehensive Handbook of Chemical Bond Energies*; CRC Press: Boca Raton, FL, 2007.

(20) Warshay, M. Shock Tube Investigation of Bromine Dissociation Rates in the Presence of Helium, Neon, Argon, Krypton, and Xenon. *J. Chem. Phys.* **1971**, *54*, 4060-4071.

(21) Ip, J. K. K.; Burns, G. Recombination of Br Atoms by Flash Photolysis over a Wide Temperature Range. II. Br_2 in He, Ne, Ar, Kr, N_2, and O_2. *J. Chem. Phys.* **1969**, *51*, 3414-3424.

(22) *Comsol Multiphysics*, Version 4.3b; Comsol, Inc.: Los Angeles, CA, 2007, available at http://www.comsol.com.

(23) Zhao, L.; Kaiser, R. I.; Xu, B.; Ablikim, U.; Ahmed, M.; Zagidullin, M. V.; Azyazov, V. N.; Howlader, A. H.; Wnuk, S. F.; Mebel, A. M. VUV Photoionization Study of the Formation of the Simplest Polycyclic Aromatic Hydrocarbon: Naphthalene ($C_{10}H_8$). *J. Phys. Chem. Lett.* **2018**, *9*, 2620–2626.

(24) Zhao L.; Kaiser, R. I.; Xu, B.; Ablikim, U.; Ahmed, M.; Evseev, M. M.; Bashkirov, E. K.; Azyazov, V. N.; Mebel, A. M. Low-Temperature Formation of Anthracene and Phenanthrene and Implications to the Synthesis of PAHs in Titan's Atmosphere. *Nature Astronomy* **2018**, *2*, DOI: 10.1038/s41550-018-0585-y.

(25) Kikoin, I. K. *Tables of Physical Quantities;* Atomizdat: Moscow, 1976.

(26) Jasper, A.W.; Pelzer, K.M.; Miller, J.A.; Kamarchik, E.; Harding, L.B.; Klippenstein, S.J. Predictive a Priori Pressure-Dependent Kinetics. *Science* **2014**, *346*, 1212-1215.

(27) Abramovich, G. N. *Applied Gasdynamics*. Nauka: Moscow, 1976.

(28) Landau, L. D.; Lifshitz, E. M. *Course of Theoretical Physics - Volume 6; Fluid Mechanics, 2nd Ed*.; Pergamon: New York, 1987.

(29) Reid, R.C.; Prausnitz, J.M.; Sherwood, T.K. *The Properties of Gases and Liquids*; McGrow-Hill: New York, 1977.

Table 1. List of reactions involved in the pyrolysis of 2-$C_{10}H_7Br$ and their rate constants.

	Reaction	Pressure, Torr	Rate constant	Units	Ref.
1f	$C_{10}H_7Br \rightarrow C_{10}H_7 + Br$	P1 = 7.5	$k_{fP1}=0.31163\times10^{24}/T^{2.4840}\exp(-42009/T) - 0.15229\times10^{99}/T^{22.363}\exp(-84077/T)$	s^{-1}	This work
		P2 = 75	$k_{fP2}=0.21831\times10^{96}/T^{22.339}\exp(-73308/T) + 0.27782\times1045/T^{8.8080}\exp(-46476/T)$	s^{-1}	This work
		7.5≤P5≤75	$k_{fP1}+(k_{fP2}-k_{fP1})\times$ (log(P1)-log(P))/(log(P1)-log(P2))	s^{-1}	This work
1r	$C_{10}H_7 + Br \rightarrow C_{10}H_7Br$	7.5≤P5≤75	$0.92836\times10^{17}/T^{7.8220}\exp(-9687.1/T) + 58.130/T^{3.7889}\exp(-1896.5/T)$	$cm^3\ s^{-1}$	This work
2f	$Br_2 \rightarrow Br+Br$		$6.18\times10^{-12}\times(T/298)^{0.5}\times \exp(-134000/8.31/T)$	s^{-1}	20
2r	$Br + Br + He \rightarrow Br_2 + He$		$3.2\times10^{-33}\times(298/T)^{1.26}$	$cm^6\ s^{-1}$	21

Table 2. Experimental conditions[24] for the measurements of pyrolysis of 2-$C_{10}H_7Br$.

Parameter	Value
He flow rate	60 μmol/s
$C_{10}H_7Br$ flow rate	5.4 nmol/s
Initial gas temperature	300 K
Output bulk pressure	10^{-6} Torr
SiC temperature[a]	1500 K

[a]At the center between molybdenum electrodes.

Table 3. Viscosity coefficients and heat capacity ratios depending on the gas temperature.[29]

gas	Viscosity, μ (g cm^{-1} s^{-1})	Heat capacity ratio, γ
He	2×10^{-4} $(T/300)^{0.5}$	1.667
C_2H_4	10^{-4} $(T/300)^{0.5}$	1.068+0.49exp(-T/300.285)
CO_2	2×10^{-4} $(T/300)^{0.5}$	1.166+0.303exp(-T/337.26)

Figure Captions

Figure 1. The gas scheme for measuring the pressure drop in the tube of the SiC chemicalreactor. PC is a personal computer; V_i denote valves, P_{in} and P_{ex} are pressure gauges located in the gas duct upstream and downstream of the tube respectively; MFC is a Mass-Flow Controller.

Figure 2. Total energy corrections for 1-bromonaphthalene ($\Delta E[\text{total}] = \Delta E[\text{geom}] + \Delta E[\text{Method}]$) calculated using two-point CBS extrapolations: black – with the cc-pVTZ and cc-pVDZ basis sets, red – with the cc-pVTZ and cc-pVQZ basis sets.

Figure 3. Calculated rate constants for dissociation of 1- (a) and 2-bromonaphthalene (b) at different pressures. Black squares – 0.01 atm, red circles – 0.0395 atm, blue triangles – 0.1 atm, magenta down-pointing triangles – 0.3 atm, green diamonds – 1 atm, purple left-pointing triangles – high pressure limit.

Figure 4. Sketch of the micro-reactor: 1 - SiC tube, 2 - molybdenum electrodes, 3 - alumina holder, 4 - copper heat exchanger, 5 - graphite slivers.

Figure 5. CFD simulation of distributions of pressure P, temperature T, and axis velocity U_0 for the gas stream along the axis of the micro-reactor under the experimental conditions. z = 0 corresponds to the inlet of SiC tube. The gray rectangles illustrate positions of the electrodes. The dashed line represents the temperature distribution for λ = 2 W m^{-1} K^{-1}.

Figure 6. CFD calculation of the 1-$C_{10}H_7Br$ pyrolysis efficiency along the axis of the micro-reactor for temperatures T = 1500 (solid curve) and 1600 K (dashed curve) at the point of the reactor's wall between the electrodes.

Figure 7. Inlet pressure dependences versus the CO_2 flow rate at ambient temperature measured experimentally (■) and calculated with Eq. (6) (●) and CFD simulations (▲).

Figure 8. Inlet pressure dependences versus the He flow rate at ambient temperature measured experimentally (■) and calculated with Eq. (6) (●) and CFD simulations (▲).

Figure 9. Calculated pressure distributions along the flow at T = 1500 K and g = 400 sccm for two carrier gases, C_2H_4 and He.

Figure 10. Residence time as a function of the gas flow rate for L = 1 cm and the gas temperature of 1000 K for He, C_2H_4, and CO_2.

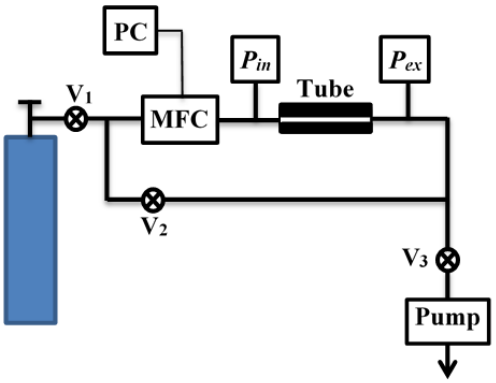

Figure 1. The gas scheme for measuring the pressure drop in the tube of the SiC chemical reactor. PC is a personal computer; V_i denote valves, P_{in} and P_{ex} are pressure gauges located in the gas duct upstream and downstream of the tube respectively; MFC is a Mass-Flow Controller.

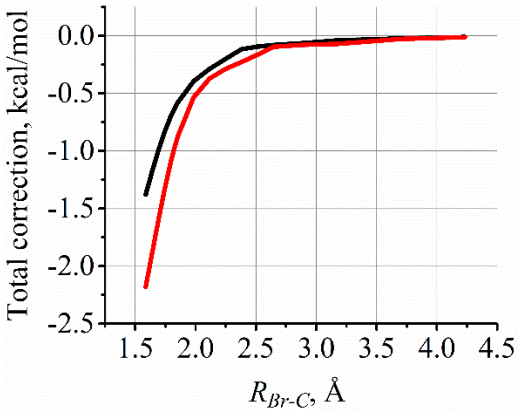

Figure 2

Figure 2. Total energy corrections for 1-bromonaphthalene ($\Delta E[\text{total}] = \Delta E[\text{geom}] + \Delta E[\text{Method}]$) calculated using two-point CBS extrapolations: black – with the cc-pVTZ and cc-pVDZ basis sets, red – with the cc-pVTZ and cc-pVQZ basis sets.

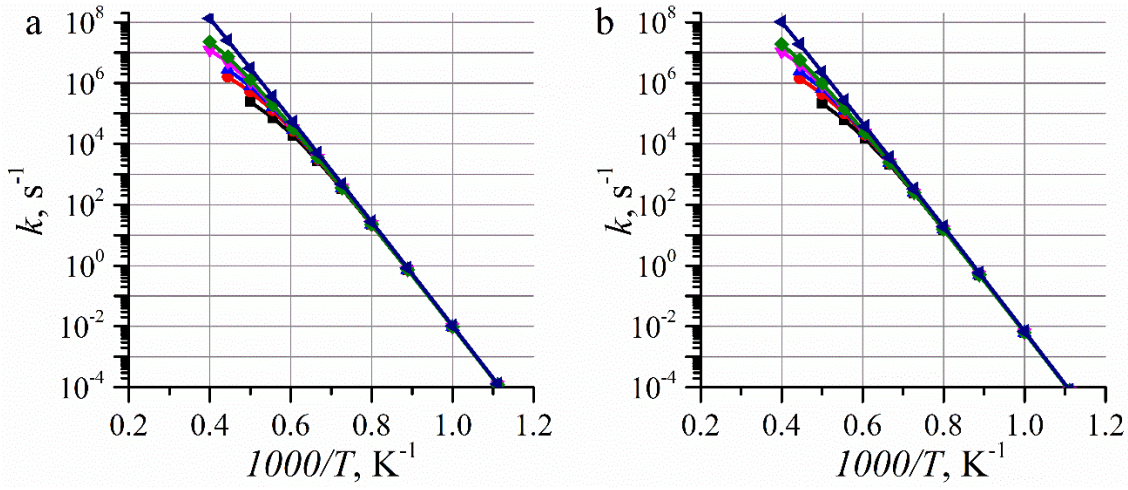

Figure 3

Figure 3. Calculated rate constants for dissociation of 1- (a) and 2-bromonaphthalene (b) at different pressures. Black squares – 0.01 atm, red circles – 0.0395 atm, blue triangles – 0.1 atm, magenta down-pointing triangles – 0.3 atm, green diamonds – 1 atm, purple left-pointing triangles – high pressure limit.

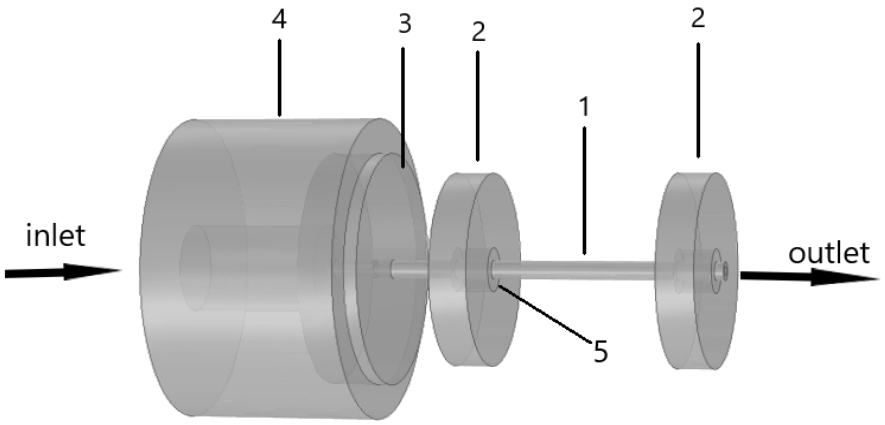

Figure 4

Figure 4. Sketch of the micro-reactor: 1 - SiC tube, 2 - molybdenum electrodes, 3 - alumina holder, 4 - copper heat exchanger, 5 - graphite slivers.

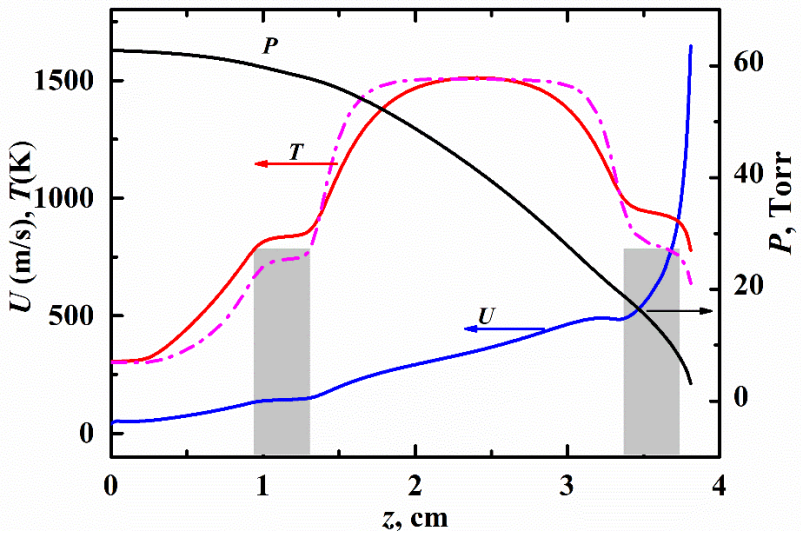

Figure 5

Figure 5. CFD simulation of distributions of pressure P, temperature T, and axis velocity U_0 for the gas stream along the axis of the micro-reactor under the experimental conditions. z = 0 corresponds to the inlet of SiC tube. The gray rectangles illustrate positions of the electrodes. The dashed line represents the temperature distribution for λ = 2 W m^{-1} K^{-1}.

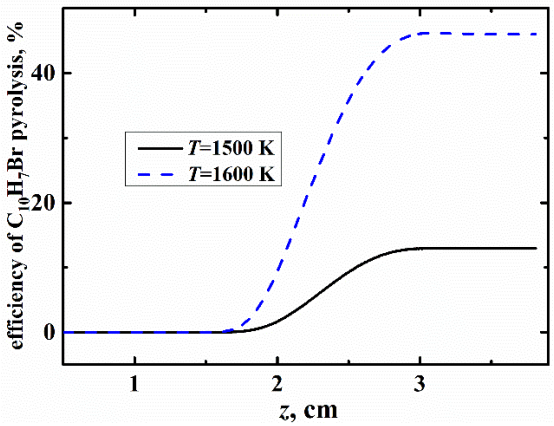

Figure 6

Figure 6. CFD calculation of the 1-$C_{10}H_7Br$ pyrolysis efficiency along the axis of the micro-reactor for temperatures T = 1500 (solid curve) and 1600 K (dashed curve) at the point of the reactor's wall between the electrodes.

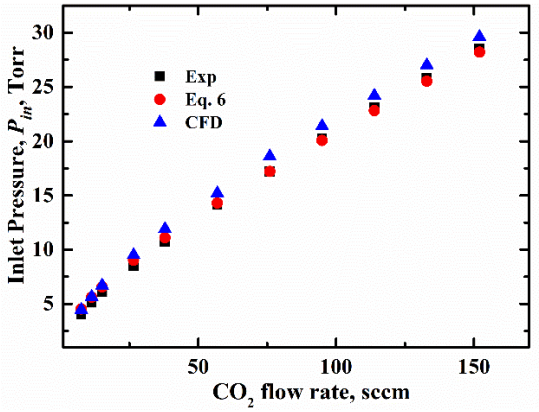

Figure 7

Figure 7. Inlet pressure dependences versus the CO_2 flow rate at ambient temperature measured experimentally (■) and calculated with Eq. (6) (●) and CFD simulations (▲).

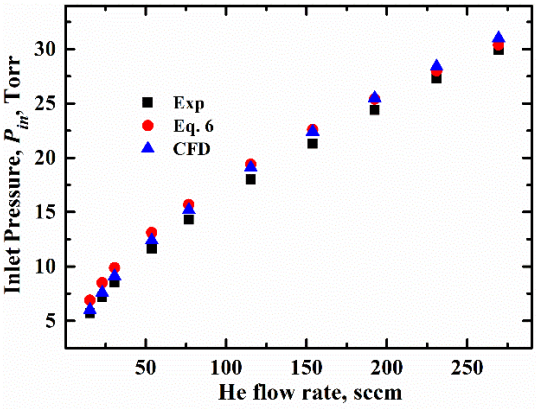

Figure 8

Figure 8. Inlet pressure dependences versus the He flow rate at ambient temperature measured experimentally (■) and calculated with Eq. (6) (●) and CFD simulations (▲).

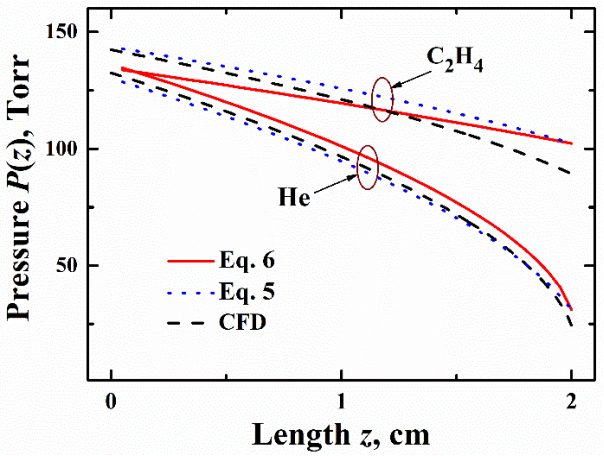

Figure 9

Figure 9. Calculated pressure distributions along the flow at T = 1500 K and g = 400 sccm for two carrier gases, C_2H_4 and He.

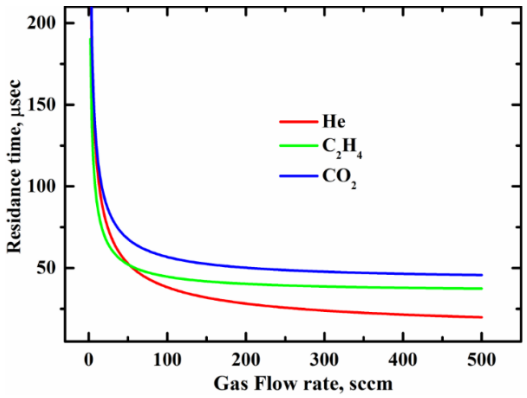

Figure 10

Figure 10. Residence time as a function of the gas flow rate for L = 1 cm and the gas temperature of 1000 K for He, C_2H_4, and CO_2.

TOC Graphic

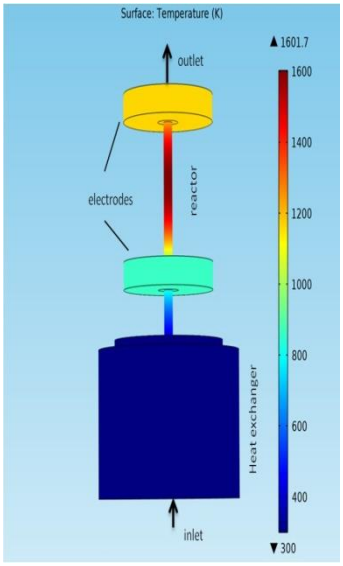
Surface: Temperature (K)
▲1601.7
1600
1400
1200
1000
800
600
400
▼300
outlet
electrodes
reactor
Heat exchanger
inlet